IEEE Access
Multidisciplinary | Rapid Review | Open Access Journal

Received November 18, 2019, accepted December 2, 2019, date of publication December 6, 2019,
date of current version December 23, 2019.

Digital Object Identifier 10.1109/ACCESS.2019.2958141

A Spare Support Vector Machine Based Fault Detection Strategy on Key Lubricating Interfaces of Axial Piston Pumps

SHIQI XIA[1], JUNHUI ZHANG[1], SHAOGAN YE[1,2], BING XU[1], WEIDI HUANG[1], AND JIAWEI XIANG[3], (Member, IEEE)

[1]State Key Laboratory of Fluid Power and Mechatronic Systems, Zhejiang University, Hangzhou 310027, China
[2]School of Aerospace Engineering, Xiamen University, Xiamen 361102, China
[3]College of Mechanical and Electrical Engineering, Wenzhou University, Wenzhou 325000, China

Corresponding author: Junhui Zhang (benzjh@zju.edu.cn)

This work was supported in part by the National Natural Science Foundation of China under Grant 51835009 and Grant 51890882, and in part by the National Key Research and Development Program of China under Grant 2018YFB2001100.

ABSTRACT Fault detection of axial piston pumps is of great significance to improve the reliability and life of fluid power systems. However, it is difficult to detect multiple faults on key lubricating interfaces due to the liquid-solid coupling. This paper proposes a fault detection strategy of the three key lubricating interfaces based on the one against all (OAA) and spare support vector machine (SSVM). The parameter sparsity is imposed to deal with the performance degradation of OAA-SVM model as a result of the imbalanced dataset. Experimental investigations on the benchmark dataset and axial piston pumps are carried out. Results show that the OAA-SSVM model accuracies of the benchmark dataset and axial piston pump are 96.67% and 95.83%, respectively, which are better than the OAA-SVM model. The recall rates of the bearing fault 3 and pump fault 2 can decrease by 13.33% and 10.00%, respectively. And the false discovery rates of the normal bearing and normal pump can be reduced by up to 7.58% and 6.24%, respectively. Besides, the OAA-SSVM model can improve the feature sparsity. Results show that the proposed method is effective in detecting multiple faults of axial piston pumps.

INDEX TERMS Axial piston pumps, multiple fault detection, one against all, spare support vector machine.

I. INTRODUCTION

The fluid power system plays an important role in the applications of the industrial hydraulics and mobile hydraulics with the advantage of high power density [1]–[3]. An axial piston pump is the critical power source of the fluid power system. Its failure may cause the system breakdown and economic losses [4]–[6].

The typical configuration of an axial piston pump is shown in Fig. 1. There are three key lubricating interfaces, which are marked using the red dotted lines: the interface between the swash plate and slipper, the interface between the piston and cylinder block, and the interface between the cylinder block and valve plate [7]–[9]. During rotation, oil films form in these interfaces. And these thin oil films work as a key bearing and sealing part in an axial piston pump [10]. Common faults on these lubricating interfaces include the slipper wear, piston wear, cavitation, etc [11].

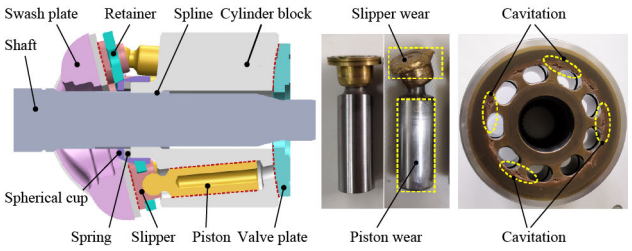

FIGURE 1. Typical configuration and common faults of an axial piston pump.

Many literatures have been developed for the fault diagnosis of axial piston pumps. These literatures can be divided into four main categories: model-based, signal processing-based, artificial intelligence-based, and hybrid methods. Recently, the latter two methods are more widely used. A method based on the convolutional neural network [12] and image

The associate editor coordinating the review of this manuscript and approving it for publication was Yanzheng Zhu.

recognition based method [13] were proposed to detect the wear faults of the interface between the slipper and swash plate, and the valve plate. The fault of worn slippers was detected through the cyclostationary analysis [14] and extreme learning machine [15]. Rolling bearings faults of axial piston pump were detected by the minimum entropy deconvolution based on simulation-determined bandpass filter [16], [17]. Loose slipper and slipper abrasion were predicted through a modified echo state networks model [18]. The fault of one single piston loose shoes was detected through the intermittent chaos and sliding window symbol sequence statistics [19]. The fuzzy C means clustering algorithm was employed to identify faults of the worn swash plate, loose piston shoe, and worn piston shoe [20]. Fault features of the loose slipper, slipper wear, and center spring wear were extracted by the local mean decomposition and improved adaptive multiscale morphology analysis [21]. The layered clustering algorithm was presented to classify the five faults abrasion of valve plate, insufficient inlet pressure, roller bearing wear, swash plate eccentricity, and clearance increases between piston and slipper [22]. There will be complex liquid-solid coupling between the three key lubricating interfaces, and this coupling makes it is difficult to detect the multiple faults on these interfaces.

The support vector machine (SVM) has been widely employed as a fault classifier of rotating machineries due to its simpler structure, better generalization ability, and faster classification speed [23], [24]. The SVM is originally used for binary classification while most cases in practice are multiclass classification [25]. Many strategies have been proposed to extend the binary SVM to multiclass classification. The common strategies include ''one against all (OAA)'', ''one against one (OAO)'', and ''direct acyclic graph (DAG)''. For the OAA method, it constructs m SVM submodels when solving the classification problem with m classes. For the OAO method and DAG method, m (m-1)/2 SVM submodels are combined to deal with the m classes problem. The OAA method is with a better classification speed due to a less number of SVM submodels in comparison to the OAO method and DAG method. It should be pointed out that when constructing the single SVM submodel, there will be imbalanced training dataset. This imbalance may diminish the classification robustness and decline the model accuracy.

In this paper, the OAA and spare support vector machine (SSVM) based method for the multiple fault detection of the three key lubricating interfaces is proposed, where parameter sparsity is imposed to deal with the effects of the imbalanced dataset. The remaining sections of this paper are organized as follows. Firstly, theoretical background is introduced in section II. Secondly, the flowchart of the OAA-SSVM methodology is presented in section III. Then, application on the benchmark dataset is conducted in section IV. The experimental investigation on axial piston pumps is carried out in section V. Finally, conclusions and future works are given in section VI.

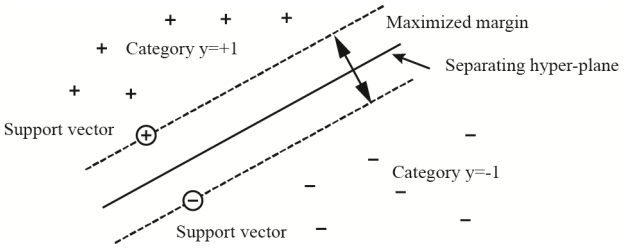

FIGURE 2. Description of the SVM algorithm.

II. THEORETICAL BACKGROUND

A. SVM ALGORITHM

As shown in Fig. 2, the aim of the SVM for the binary classification is to find a separating hyper-plane, which can separate the dataset (x_i, $i = 1, 2, \ldots, N$) into two categories ($y_i = \pm 1$) with the maximized margin. + indicating data points of class +1, and − indicating data points of class –1. The data points used to construct the separating hyper-plane are called support vectors.

The parameters of the separating hyper-plane, (ω, b), can be calculated as follows.

$$(\omega, b) \in \arg\min \frac{1}{2} \|\omega\|_2^2 + C \sum_{n=1}^{N} H_{\omega,b}(x_i, y_i) \tag{1}$$

where ω and b refer to an N-dimensional vector and a scalar. C represents the regularization parameter, which adjusts the trade-off between the misclassification rate and dataset sparsity. $H_{\omega,b}(x_i, y_i)$ denotes the hinge loss function, which equals $\max\{0, 0, 1-y_i(\omega^{\mathrm{T}}x_i+\mathrm{b})\}$.

B. SSVM ALGORITHM

The SVM algorithm may promote the dataset sparsity because only a few features actually contribute to defining the parameters (ω, b). In addition, the large class imbalance may weaken the dataset sparsity and diminish the classification robustness. The SSVM was proposed to accomplish the feature selection and classification jointly. The SSVM algorithm can induce the parameter sparsity by imposing a ℓ_1 norm to the first term of (1). And a square hinge loss function, $H^2_{\omega,b}(x_i, y_i)$, is imposed on the penalization term of (1). In order to deal with imbalanced dataset, the penalization term consists of two weighted sums of the imbalanced dataset. The separating hyper-plane, (ω, b), can be calculated as follows.

$$(\omega, b) \in \arg\min \|\omega\|_1 + C \sum_{n=1}^{N_{-1}} H^2_{\omega,b}(x_i, y_i) + C \frac{N_{-1}}{N_{+1}} \sum_{n=1}^{N_{+1}} H^2_{\omega,b}(x_i, y_i) \tag{2}$$

where N_{-1} and N_{+1} are the numbers of the two class.

In order to deal with the non-differentiable optimization problems of the ℓ_1 norm in the SSVM, the forward backward splitting algorithm was utilized, where the proximity operator of the ℓ_1 norm was calculated on a gradient descent step of

the square hinge loss function.

$$\mathrm{Pro}[l_1\ \mathrm{norm}(\omega_{l_1})] = \arg\min \frac{1}{2}\left\|\omega_{l_1}-\omega\right\|_2^2 + l_1\ \mathrm{norm}(\omega_{l_1}) \quad (3)$$

The parameter ω at the z^{th} iteration can be calculated as follows.

$$\omega^z = \mathrm{Pro}[\omega^{z-1} - \frac{1}{D}\nabla H^2_{\omega,b}(\omega^{z-1})] \quad (4)$$

where D refers to a constant of gradient descent step, $\nabla H^2_{\omega,b}$ denotes the Lipschitz-continuous gradient of the square hinge loss function.

C. OAA ALGORITHM

In the OAA strategy, the m^{th} model ($m = 1, 2 \ldots,$ M) is trained with the specified dataset where the labels of the m^{th} class are set with $+1$ and the labels of other classes are set with -1. Then, the parameters $(\omega, \mathrm{b})_m$ of the separating hyper-plane of the m^{th} model are obtained. The testing dataset is fed to the m^{th} trained model. A voting strategy of the testing results is utilized to determine the predicted results of all m models, where if the testing results show the dataset is in the m^{th} class, then the vote of this class is added by one, on the contrary, the vote of other classes is increased by one. The predicted class is decided according to the maximum vote. In condition that some classes own equal vote, the class with a lower index is chosen as the predicted result. This strategy is called the ''Max Wins'' criterion.

III. PROPOSED METHOD

A. OAA-SSVM METHODOLOGY FOR MULTIPLE FAULT DETECTION

In the traditional OAA-SVM model, the dataset is imbalanced when training the m^{th} submodel. And the SVM is only suitable for the balanced training dataset. The minority samples of the imbalanced dataset will be distorted due to the sub-optimal classification of the SVM. In order to deal with the accuracy decline caused by the imbalanced dataset, a multiple fault detection methodology based on the SSVM algorithm is proposed, which can improve the classification robustness of dataset with large class imbalance [26]. Details of the OAA-SSVM methodology are shown in Fig. 3. Firstly, raw vibration information is picked up from the diagnostic objects by the signal collection module. Different features revealing fault characteristics are extracted from the raw vibration signal. The dataset with extracted features is divided into the training dataset and testing dataset independently. The training dataset with multi faults is fed to the OAA-SSVM model. During the training process of the m^{th} SSVM submodel, the training labels of the m^{th} class are set with $+1$ while the labels of other class are set with -1. After training, m SSVM submodels with hyper-plane parameters $(\omega, \mathrm{b})_1$, $(\omega, \mathrm{b})_2$, …, $(\omega, \mathrm{b})_m$ are constructed. Then, the testing dataset is employed to test the trained OAA-SSVM submodels in turn. Testing results from m SSVM submodels are synthesized based on the ''Max Wins'' criterion. At last, the predicted results of the OAA-SSVM model are determined.

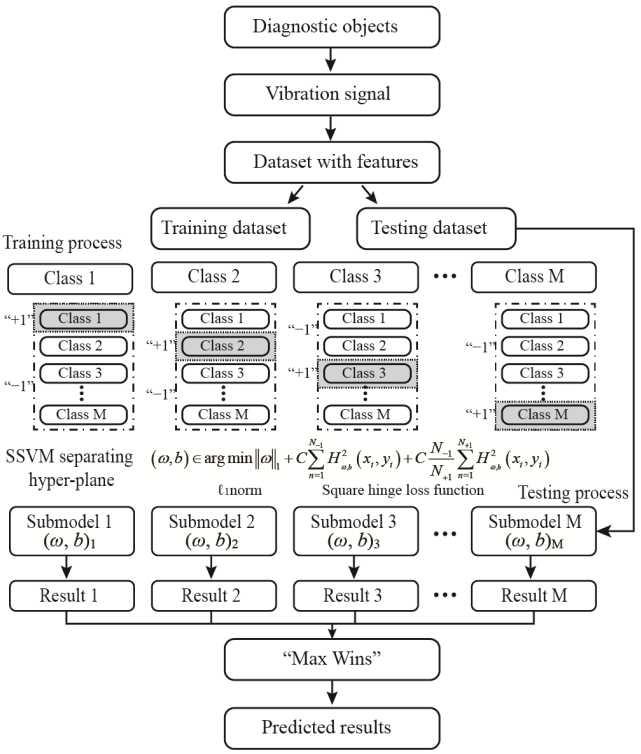

FIGURE 3. Flowchart of the OAA-SSVM methodology.

B. STATISTICAL FEATURE EXTRACTION

In order to capture the weak fault characteristics embedded in the background noise, 20 features extracted by the signal processing techniques in the time domain, frequency domain, and time-frequency domain are listed in Table. 1. These features are selected based on our prior knowledge. And they can reveal the fault characteristics from different aspects. The features F_1-F_6 are calculated from the time domain waveforms. $x(n)$ $(n = 1, 2, \ldots, N)$ is the raw vibration signal in the time domain and N denotes the data length. F_1 and F_2 are the root amplitude and root mean square, respectively, which are related to the signal energy. F_3, F_4, F_5, and F_6 refers to the kurtosis value, crest factor, clearance factor, and impulse factor, respectively. They are sensitive to the impulse information [27]. The features F_7-F_{12} are extracted from the frequency spectrum obtained through the Fourier transform [28], [29]. $s(k)$ and $f(k)$ $(k = 1, 2, \ldots, K)$ denote the amplitude and frequency of the k^{th} spectrum line, respectively. K is the spectrum line number. F_7, F_8, and F_9 can reveal the location of the main frequency in the spectrum. The convergence characteristics of the spectrum power are reflected by features F_{10}, F_{11}, and F_{12}. s_1 refers to the frequency center. It can be calculated as follows.

$$s_1 = \sum_{k=1}^{K} f(k)\, s(k) \Big/ \sum_{k=1}^{K} s(k) \quad (5)$$

The collected vibration signals are not always stationary due to the fault impact [30]–[32]. The wavelet packet transform (WPT) has been widely used to deal with the

TABLE 1. Specifications of the statistical features.

Specifications	Specifications
$F_1=\left[\frac{1}{N}\sum_{n=1}^{N}\sqrt{\lvert x(n)\rvert}\right]^2$	$F_2=\sqrt{\frac{1}{N}\sum_{n=1}^{N}x(n)^2}$
$F_3=\frac{1}{(N-1)x_{std}^4}\sum_{n=1}^{N}\left[x(n)-x_{mean}\right]^4$	$F_4=\max\lvert x(n)\rvert\Big/\sqrt{\frac{1}{N}\sum_{n=1}^{N}x(n)^2}$
$F_5=\max\lvert x(n)\rvert\Big/\left[\frac{1}{N}\sum_{n=1}^{N}\sqrt{\lvert x(n)\rvert}\right]^2$	$F_6=N\max\lvert x(n)\rvert\Big/\sum_{n=1}^{N}\lvert x(n)\rvert$
$F_7=\frac{1}{K}\sum_{k=1}^{K}s(k)$	$F_8=\sqrt{\sum_{k=1}^{K}f^4(k)s(k)\Big/\sum_{k=1}^{K}f^2(k)s(k)}$
$F_9=\sum_{k=1}^{K}f^2(k)s(k)\Big/\sqrt{\sum_{k=1}^{K}f^4(k)s(k)\sum_{k=1}^{K}s(k)}$	$F_{10}=\sqrt{\frac{1}{K}\sum_{k=1}^{K}\left[f(k)-s_1\right]^2s(k)}\Big/s_1$
$F_{11}=\frac{1}{Ks_1^4F_{10}^4}\sum_{k=1}^{K}\left[f(k)-s_1\right]^4s(k)$	$F_{12}=\frac{1}{K\sqrt{s_1F_{10}}}\sum_{k=1}^{K}\lvert f(k)-s_1\rvert^{1/2}s(k)$
$F_{13}=\sum_{j=1}^{2^{-m}N}\left[x_1(j)\right]^2\Big/\sum_{i=1}^{2^m}\sum_{j=1}^{2^{-m}N}\left[x_i(j)\right]^2$	$F_{14}=\sum_{j=1}^{2^{-m}N}\left[x_2(j)\right]^2\Big/\sum_{i=1}^{2^m}\sum_{j=1}^{2^{-m}N}\left[x_i(j)\right]^2$
$F_{15}=\sum_{j=1}^{2^{-m}N}\left[x_3(j)\right]^2\Big/\sum_{i=1}^{2^m}\sum_{j=1}^{2^{-m}N}\left[x_i(j)\right]^2$	$F_{16}=\sum_{j=1}^{2^{-m}N}\left[x_4(j)\right]^2\Big/\sum_{i=1}^{2^m}\sum_{j=1}^{2^{-m}N}\left[x_i(j)\right]^2$
$F_{17}=\sum_{j=1}^{2^{-m}N}\left[x_5(j)\right]^2\Big/\sum_{i=1}^{2^m}\sum_{j=1}^{2^{-m}N}\left[x_i(j)\right]^2$	$F_{18}=\sum_{j=1}^{2^{-m}N}\left[x_6(j)\right]^2\Big/\sum_{i=1}^{2^m}\sum_{j=1}^{2^{-m}N}\left[x_i(j)\right]^2$
$F_{19}=\sum_{j=1}^{2^{-m}N}\left[x_7(j)\right]^2\Big/\sum_{i=1}^{2^m}\sum_{j=1}^{2^{-m}N}\left[x_i(j)\right]^2$	$F_{20}=\sum_{j=1}^{2^{-m}N}\left[x_8(j)\right]^2\Big/\sum_{i=1}^{2^m}\sum_{j=1}^{2^{-m}N}\left[x_i(j)\right]^2$

non-stationary signals in the time-frequency domain [33]. The WPT owns a good resolution in both low and high frequency domain by matching the frequency band adaptively. Hence, apart from the features extracted in the time domain or frequency domain, features F_{13}-F_{20} are utilized to represent the subband energy ratio. $x_i(j)$ $(i = 1, 2, \ldots, 8)$ is the i^{th} subband decomposed by the WPT. m denotes the decomposition level (typically $m = 3$).

IV. APPLICATION ON THE BENCHMARK DATASET

A. DESCRIPTIONS OF THE BENCHMARK DATASET

In this section, the OAA-SSVM methodology is applied to the benchmark dataset, which is provided by the bearing data center website of the Case Western Reserve University [34]. The test rig of the benchmark dataset is shown in Fig. 4, which consists of an electric motor, a torque transducer, and a dynamometer. Single point faults (0.007 inches) were introduced at the inner raceway (fault 1), rolling element (fault 2), and outer raceway (fault 3) of the bearing through the electro-discharge machining. The motor load was 0 horsepower and the speed was around 1796 r/min. Drive end bearing vibration data were collected with the sampling frequency being 48000 Hz.

Vibration signals and corresponding spectrums of the four bearing conditions (normal bearing, fault 1, fault 2, and fault 3) are shown in Fig. 5, respectively.

The length of the time domain waveform is 24000 points (0.50 s). The frequency of spectrums ranges from 0 Hz to 6000 Hz. It is found that the amplitudes of the four bearing conditions are different. The amplitudes of the normal bearing, fault 1, fault 2, and fault 3 are around 0.25, 3, 0.6, and 1.5, respectively. The frequency spectrums of the four bearing conditions are shown in Fig. 5 (b), (d), (f), and (h),

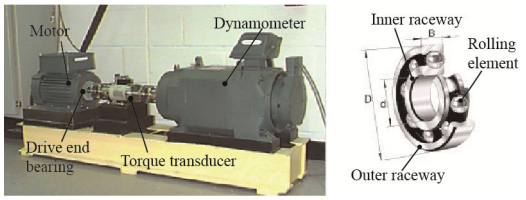

FIGURE 4. Test rigs of the benchmark dataset.

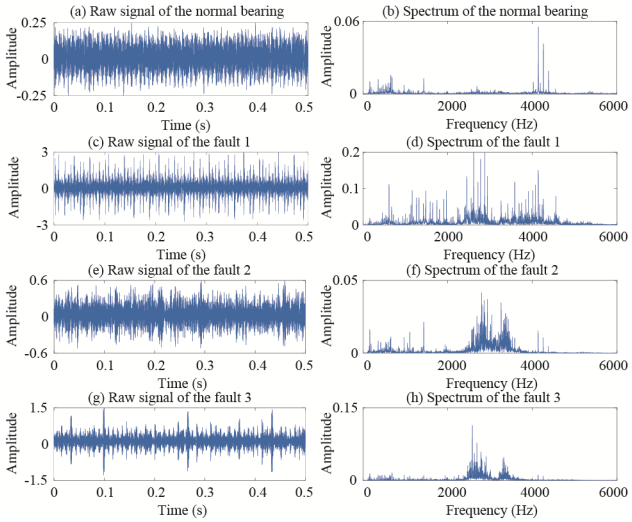

FIGURE 5. Vibration signals and corresponding spectrums of the four bearing conditions.

respectively. Vibration amplitudes of the normal bearing are mainly concentrated in the frequency band 0-1000 Hz and 4000-4500 Hz. The spectrum distribution of the fault 1 is wider than that of the other conditions, which ranges from 400 Hz to 4500 Hz. The amplitudes of the fault 2 are mainly located in the frequency band 0-1500 Hz and 2500-4400 Hz. The amplitudes of the fault 3 are mainly concentrated in the frequency band 2500-3500 Hz.

For each bearing condition, 100 samples were constructed as the training dataset and 30 samples were employed as the testing dataset. The length of single sample was 512 points. During the process of statistical features extraction, the wavelet function, sym4, was used. 20 features F_1-F_{20} of the training dataset under four bearing conditions are shown in Fig. 6. As can be seen from Fig. 6 (a), (b), (g), and (j), four bearing conditions can be distinguished using features F_1, F_2, F_7, and F_{10}, obviously. The normal bearing and the fault 1 can be detected using the features F_{16} as shown in Fig. 6 (p). In Fig. 6 (c), (d), (e), (f), (i), (k), (l), (o), (s), and (t), the features F_3, F_4, F_5, F_6, F_{11}, and F_{12} of the fault 1 are different from other conditions. And features F_9, F_{15}, F_{19}, and F_{20} of the normal bearing are different from other three conditions. Features F_8, F_{13}, F_{14}, F_{17}, and F_{18} are shown in Fig. 6 (h), (m), (n), (q), and (r), respectively, and no feature differences can be identified among the four bearing conditions.

B. PERFORMANCE ASSESSMENT

Model performance of the OAA-SVM methodology and OAA-SSVM methodology is compared in the application

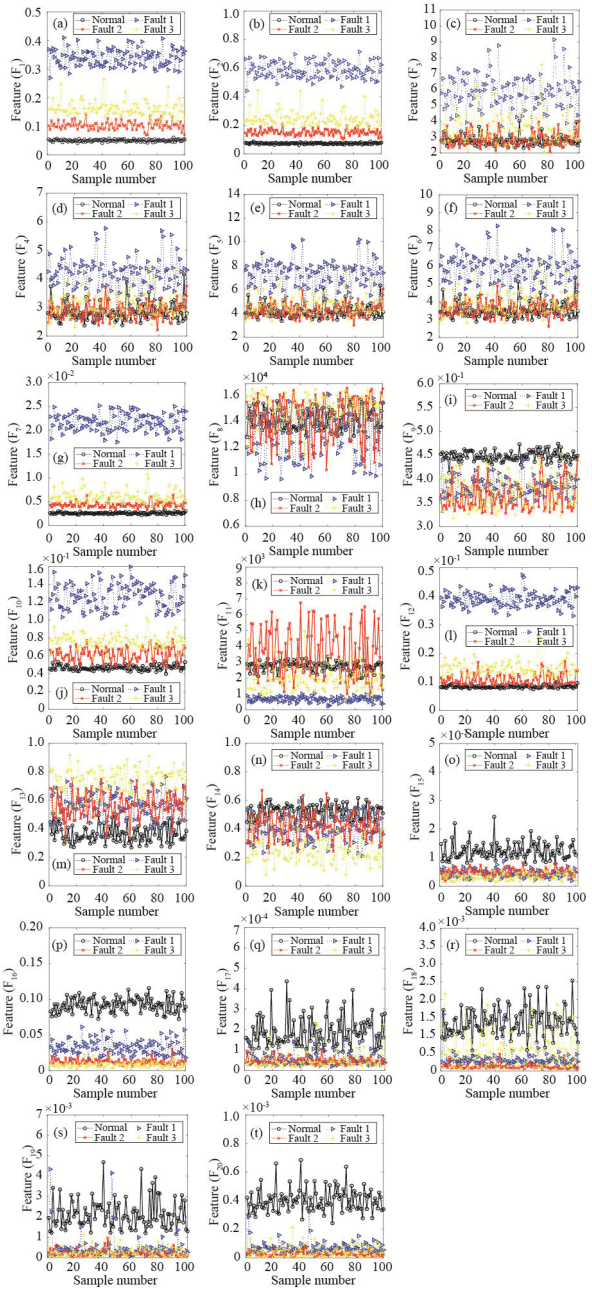

FIGURE 6. Comparisons of the 20 features between the normal bearing, fault 1, fault 2, and fault 3.

of the benchmark dataset. Results of these two models are shown in Fig. 7. The ordinate represents the model accuracies $\mathrm{Acc_{tr}}$(calculated from the training dataset) and $\mathrm{Acc_{te}}$ (calculated from the testing dataset). And the abscissa indicates the regularization parameter C. It ranges from 1.00×10^{-3} to 1.00×10^{2}, which is given on a logarithmic scale. As can be seen from Fig. 7 (a), the training accuracy $\mathrm{Acc_{tr}}$ increases with the increase of C due to the fact that a larger C can reduce the misclassification rate. There is an intersection point when C is around 2.31×10^{-2}. The maximum $\mathrm{Acc_{tr}}$ 100.00% of the OAA-SVM model and OAA-SSVM model occurs when C is around 3.05 and 1.23×10^{1}, respectively. The testing

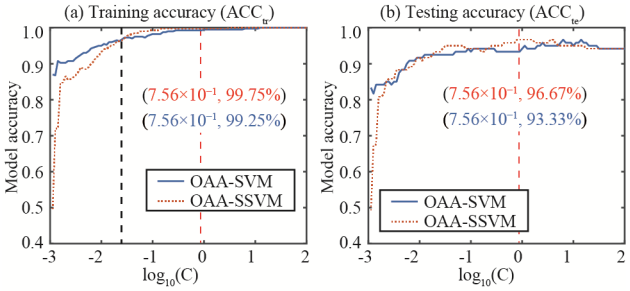

FIGURE 7. OAA-SVM and OAA-SSVM model accuracies $\mathrm{Acc_{tr}}$ and $\mathrm{Acc_{te}}$ for the bearing.

TABLE 2. $\mathrm{Acc_{tr}}$ and $\mathrm{Acc_{te}}$ for the bearing with $C = 7.56 \times 10^{-1}$.

Model	OAA-SVM	OAA-SSVM	Δ
Training accuracy ($\mathrm{Acc_{tr}}$)	99.25%	99.75%	0.50%
Testing accuracy ($\mathrm{Acc_{te}}$)	93.33%	96.67%	3.34%

accuracy $\mathrm{Acc_{te}}$ is shown in Fig. 7 (b). The maximum $\mathrm{Acc_{te}}$ of the OAA-SSVM model is 96.67%. It occurs when C is around 7.56×10^{-1}. And the $\mathrm{Acc_{te}}$ is with no further increase as C increases. The optimized C was chosen as 7.56×10^{-1} based on the criterion that a minimum C makes the model accuracy, $\mathrm{Acc_{te}}$, to be the largest while avoiding the issue of the over-fitting. The model accuracies $\mathrm{Acc_{tr}}$ and $\mathrm{Acc_{te}}$ for the bearing with $C = 7.56 \times 10^{-1}$ are shown in Table. 2. The training accuracies $\mathrm{Acc_{tr}}$ of the OAA-SVM model and OAA-SSVM model are 99.25% and 99.75%, respectively. And the testing accuracies $\mathrm{Acc_{te}}$ of these two models are 93.33% and 96.67%, respectively. Comparing to the OAA-SVM model, the $\mathrm{Acc_{tr}}$ and $\mathrm{Acc_{te}}$ of the OAA-SSVM model can increase by 0.50% and 3.34%, respectively.

Confusion matrices of the training and testing dataset are shown in Fig. 8 with $C = 7.56 \times 10^{-1}$. As can be seen from Fig. 8 (a) and (b), for the training dataset of the OAA-SVM model, the recall rates of the normal bearing, fault 1, fault 2, and fault 3 are 100.00%, 100.00%, 100.00%, and 97.00%, respectively. The false discovery rates of these four conditions are 1.96%, 0.00%, 0.99%, and 0.00%, respectively. For the testing dataset of the OAA-SVM model, the recall rates of the normal bearing, fault 1, fault 2, and fault 3 are 100.00%, 100.00%, 96.67%, and 76.67%, respectively. The false discovery rates are 16.67%, 0.00%, 6.45%, and 0.00%, respectively. The OAA-SSVM model confusion matrices are shown in Fig. 8 (c) and (d). For the training dataset, the recall rates of the normal bearing, fault 1, fault 2, and fault 3 are 100.00%, 100.00%, 100.00%, and 99.00%, respectively. The false discovery rates are 0.00%, 0.00%, 0.99%, and 0.00%, respectively. For the testing dataset of the OAA-SSVM model, the recall rates are 100.00%, 100.00%, 96.67%, and 90.00%, respectively. The false discovery rates are 9.09%, 0.00%, 3.33%, and 0.00%, respectively. The false discovery rate of the normal bearing is the highest due to the "Max Wins" criterion. The confusion matrices show that the recall rate of the fault 3 in the testing dataset increases by 13.33%. In addition, the false discovery rates of the normal bearing

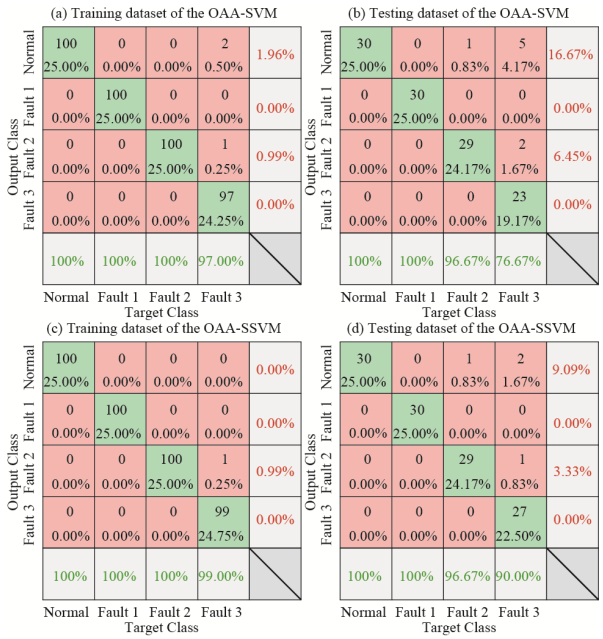

FIGURE 8. OAA-SVM and OAA-SSVM model confusion matrices of the bearing.

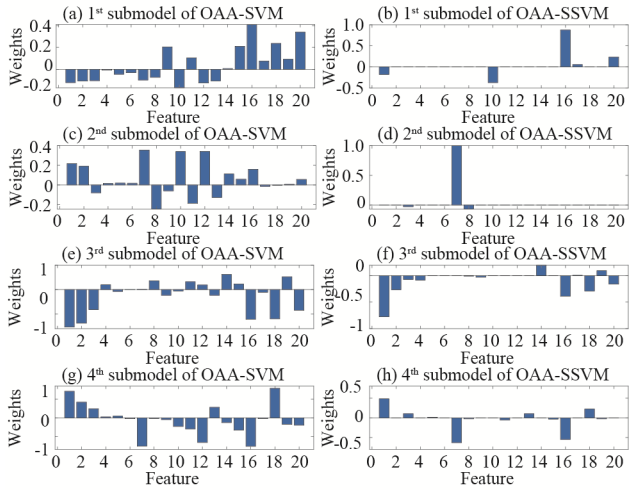

FIGURE 9. Feature weights of the four OAA-SVM and OAA-SSVM submodels with $C = 7.56 \times 10^{-1}$.

and the fault 2 in the testing dataset can be reduced by 7.58% and 3.12%, respectively.

In order to validate the feature sparsity of the OAA-SSVM methodology, feature weights of the four submodels are shown in Fig. 9. For the 1st submodel of the normal bearing, features F_1, F_{10}, F_{16}, F_{17}, and F_{20} make contributions. For the 2nd submodel of the fault 1, only features F_3, F_7, and F_8 take effect. For the 3rd submodel of the fault 2, features F_1, F_2, F_3, F_4, F_8, F_9, F_{14}, F_{16}, F_{17}, F_{18}, F_{19}, and F_{20} were included. For the 4th submodel of the fault 3, features F_1, F_3, F_5, F_7, F_8, F_{11}, F_{13}, F_{15}, F_{16}, F_{18}, and F_{19} contribute to the OAA-SSVM model. The feature number of the four submodels was reduced by 15, 17, 8, and 9, respectively. These features contributing to the OAA-SSVM submodels

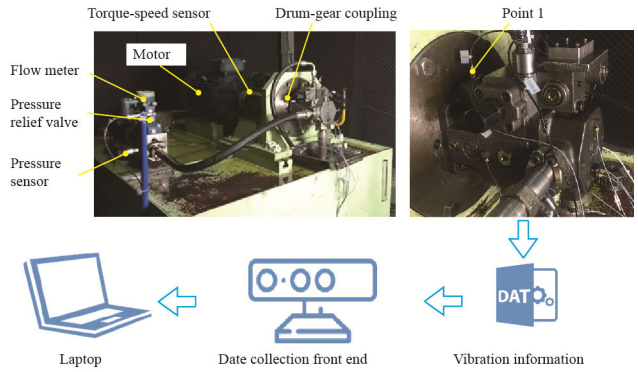

FIGURE 10. Arrangement of the testing rigs.

are useful for classification due to their differences among the four bearing conditions, which is shown in section IV-A. This indicates the OAA-SSVM methodology with the feature sparsity is effective in detecting the multiple faults of the benchmark dataset.

V. EXPERIMENTAL INVESTIGATION ON AXIAL PISTON PUMPS

A. DESCRIPTIONS OF THE TESTING PUMP AND RIGS

An experimental investigation was conducted in the axial piston pump to validate the applicability of the multiple fault detection methodology. The detailed parameters of the testing pump are described as follows [35]. The testing pump is with 9 pistons. The maximum output pressure is 35 MPa. The rated driving speed is 1500 r/min. The maximum displacement is 40 m^3/r. The overall dimension is about 333 mm × 200 mm × 230 mm.

The schematic diagram of the test rigs is shown in Fig. 10. The driving motor is connected with the testing pump through the drum-gear coupling and torque-speed sensor. The input torque and speed signals are collected by the torque-speed sensor. The input speed is controlled by the frequency converter. The output pressure of the testing pump is set by the pressure relief valve. A pressure sensor and pressure gauge are utilized to measure the output pressure. The output flow of the testing pump is monitored by a flow meter. The vibration information on point 1 is acquired by the data collection module, which consists of the data collection front end and laptop. The sampling frequency of the front end is 48000 Hz.

B. MULTIPLE FAULT ARRANGEMENTS

In this section, multiple fault arrangements on the three key lubricating interfaces of the testing pump are introduced. As shown in Fig. 11 (a), the fault of the interface between the swash plate and slipper was the failure of hydrostatic support caused by the blocked hole of the slipper (fault 1). The fault of the interface between the piston and cylinder block was the piston wear (fault 2). As shown in Fig. 11 (b), considering that the features of piston wear are weak, three pistons with 0.03 mm wear in the diameter direction were distributed on the marked positions. The fault of the interface between the

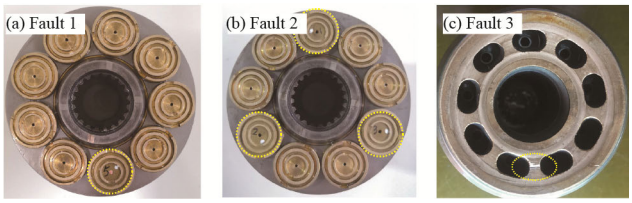

FIGURE 11. Multiple fault arrangements of the testing pump.

cylinder block and valve plate was the pitting defect (0.5 mm $\times$0.3 mm) on the surface of the cylinder block (fault 3), which is shown in Fig. 11 (c).

Vibration signals and corresponding spectrums of the four pump conditions (normal pump, fault 1, fault 2, and fault 3) are shown in Fig. 12, respectively.

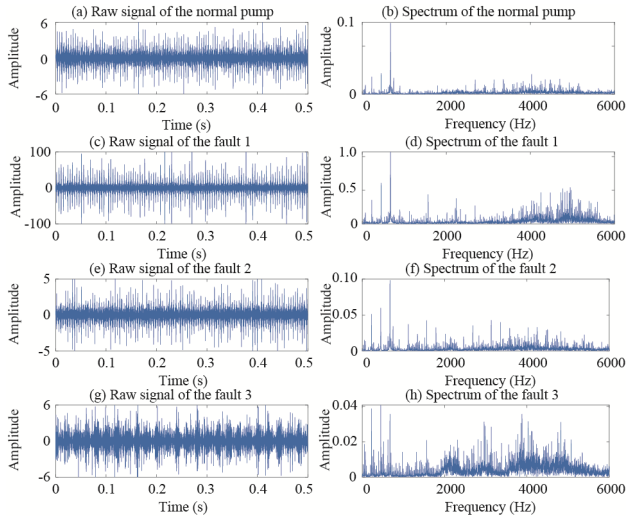

FIGURE 12. Vibration signals and corresponding spectrums of the four pump conditions.

As shown in Fig. 12 (a), (c), (e), and (g), the vibration amplitude of the fault 1 is around 100, which is larger than that of other conditions. Amplitudes of the normal pump, fault 2, and fault 3 are around 6, 5, and 6, respectively. It is hard to classify the four pump conditions based on the waveforms in the time domain. The frequency spectrums of the four pump conditions are shown in Fig. 12 (b), (d), (f), and (g), respectively. The vibration amplitudes in the piston-passing frequency and its harmonics are obvious due to the excitations from oil suction and extrusion. Some differences in the frequency spectrums can be found. For the normal pump, amplitudes are mainly concentrated in the 1st, 2nd, and 3rd order harmonics and the frequency band 3000-5000 Hz. For the fault 1, amplitudes are mainly distributed in the 1st, 2nd, 3rd, 7th, and 10th order harmonics and the frequency band 4000-5000 Hz. For the fault 2, amplitudes are mainly concentrated in the 1st, 2nd, 3rd, 5th, and 7th order harmonics and the frequency band 3000-5000 Hz. For the fault 3, amplitudes are mainly located in the 1st, 2nd, 3rd, and 7th order harmonics and the frequency band 2000-5000 Hz.

TABLE 3. Acc_{tr} and Acc_{te} for the testing pump with $C = 6.14$.

Model	OAA-SVM	OAA-SSVM	Δ
Training accuracy (Acc_{tr})	93.25%	96.00%	2.75%
Testing accuracy (Acc_{te})	93.33%	95.83%	2.50%

In order to train and test the OAA-SSVM model for multiple fault detection, the training dataset with 100 training samples and the testing dataset with 30 testing samples were constructed for the normal pump, fault 1, fault 2, and fault 3, respectively. The training dataset and testing dataset were independent. A single sample of the dataset was with 512 points. Features of single sample in the time domain and frequency domain were calculated according to the formulas described in section III-B, for the feature extraction of the WPT subbands, the wavelet function was sym4. Twenty features F_1-F_{20} of the training dataset with 100 samples were shown in Fig. 13. From Fig. 13 (h), (i), and (q), it is found that features F_8, F_9, and F_{17} of the four conditions are quite different. Fig. 13 (c), (e), (f), and (o) depict that there are a little differences between the features F_3, F_5, F_6, and F_{15} of the four conditions. As can be seen from Fig. 13 (a), (b), (g), (j), (k), and (l), the fault 1 can be distinguished among the four conditions using features F_1, F_2, F_7, F_{10}, F_{11}, and F_{12}. While, in Fig. 13 (d), (m), (n), (p), (r), (s), and (t), features F_4, F_{13}, F_{14}, F_{16}, F_{18}, F_{19}, and F_{20} flatuate with the sample number and no differences can be identified from these features of the four pump conditions.

C. PERFORMANCE ASSESSMENT

Performance of the OAA-SVM model and OAA-SSVM model is assessed in this section. Results of these two models are shown in Fig. 14. As shown in Fig. 14 (a), the training accuracy Acc_{tr} increases with the increase of C. There is an intersection point when C is around 7.56×10^{-1}. The maximum Acc_{tr} of the OAA-SSVM model and OAA-SVM model are 99.00% and 94.00%, respectively. The testing results Acc_{te} are shown in Fig. 14 (b), the maximum Acc_{te} of these two models are 95.83% and 95.00%, respectively. The maximum Acc_{te} of the OAA-SSVM model occurs when C equals 6.14. And there is no further increase of the Acc_{te} as C increases. The optimized C was chosen as 6.14 based on the criterion. The model accuracies Acc_{tr} and Acc_{te} for the testing pump with $C = 6.14$ are shown in Table. 3. The training accuracies Acc_{tr} of the OAA-SVM model and OAA-SSVM model are 93.25% and 96.00%, respectively. And the testing accuracies Acc_{te} of these two models are 93.33% and 95.83%, respectively. Comparing to the OAA-SVM model, the Acc_{tr} and Acc_{te} of the OAA-SSVM model can increase by 2.75% and 2.50%, respectively.

Confusion matrices of the training and testing dataset are shown in Fig. 15 with $C = 6.14$. As can be seen from Fig. 15 (a) and (b), for the training dataset of the OAA-SVM model, the recall rates of the normal pump, fault 1, fault 2, and fault 3 are 96.00%, 100.00%, 81.00%, and 96.00%, respectively. The false discovery rates of these four conditions

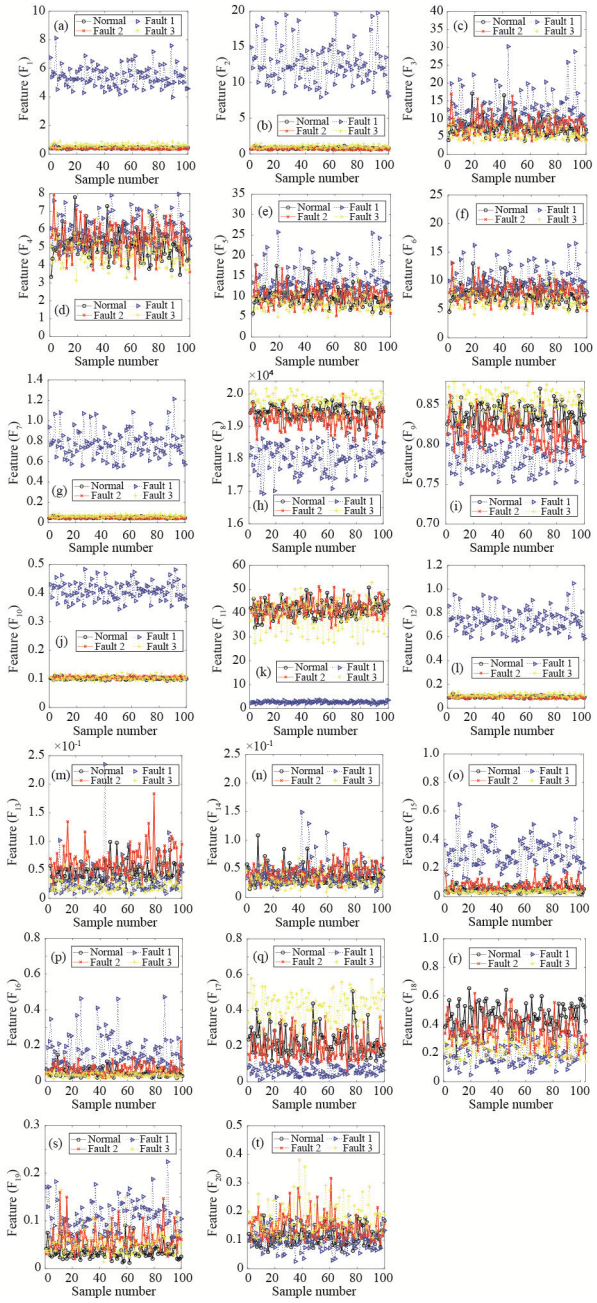

FIGURE 13. Comparisons of the 20 features between the normal pump, fault 1, fault 2, and fault 3.

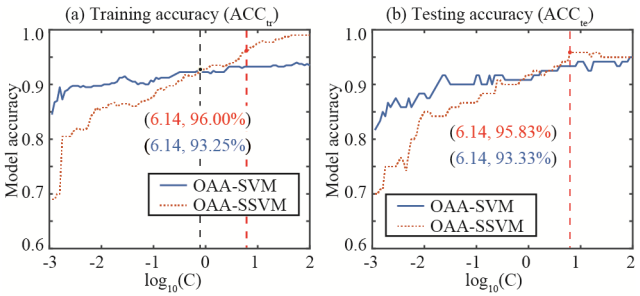

FIGURE 14. OAA-SVM and OAA-SSVM model accuracies Acc_{tr} and Acc_{te} for the testing pump.

FIGURE 15. OAA-SVM and OAA-SSVM model confusion matrices of the testing pump.

are 17.95%, 0.00%, 6.90%, and 0.00%, respectively. For the testing dataset of the OAA-SVM model, the recall rates of the normal pump, fault 1, fault 2, and fault 3 are 96.67%, 100.00%, 80.00%, and 96.67%, respectively. The false discovery rates are 17.14%, 0.00%, 7.69%, and 0.00%, respectively. The OAA-SSVM model confusion matrices are shown in Fig. 15 (c) and (d). For the training dataset, the recall rates of the normal pump, fault 1, fault 2, and fault 3 are 98.00%, 100.00%, 91.00%, and 95.00%, respectively. The false discovery rates are 11.71%, 0.00%, 3.19%, and 0.00%, respectively. For the testing dataset of the OAA-SSVM model, the recall rates are 100.00%, 100.00%, 86.67%, and 96.67%, respectively. The false discovery rates are 11.76%, 0.00%, 3.70%, and 0.00%, respectively. The false discovery rate of the normal pump is the highest due to the "Max Wins" criterion. The confusion matrices show that the recall rates of the fault 2 in the training dataset and testing dataset increase by 10.00% and 6.67%, respectively. Moreover, the false discovery rates of the normal pump in the training dataset and testing dataset decrease by 6.24% and 5.38%, respectively.

In order to validate the feature sparsity of the OAA-SSVM methodology, feature weights of the four submodels are shown in Fig. 16. For the 1st submodel of the normal pump, features F_1, F_2, F_4, F_5, F_6, F_7, F_8, F_9, F_{10}, F_{11}, F_{12}, F_{17}, F_{19}, and F_{20} make contributions. For the 2nd submodel of the fault 1, only features F_{10} and F_{14} take effect. For 3rd submodel of the fault 2, features F_1, F_2, F_3, F_5, F_6, F_9, F_{10}, F_{11}, F_{12}, F_{15}, and F_{20} are included. For the 4th submodel of the fault 3, features F_3, F_4, F_8, F_9, F_{13}, F_{14}, F_{16}, F_{18}, F_{19}, and F_{20} contribute to the OAA-SSVM model. The feature

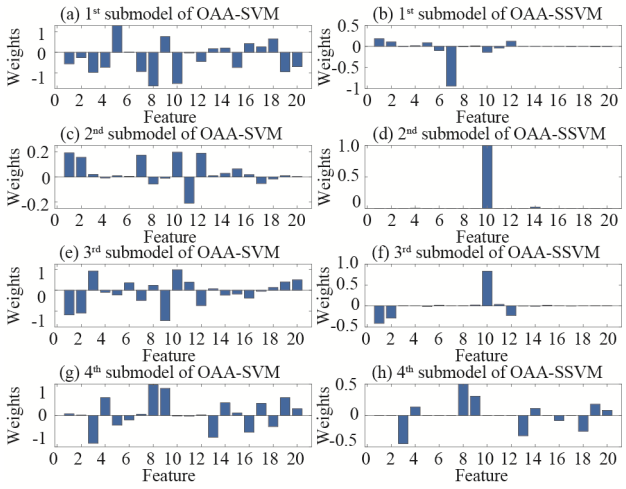

FIGURE 16. Feature weights of the four OAA-SVM and OAA-SSVM submodels with $C = 6.14$.

number of the four submodels can be reduced by 6, 18, 9, and 10, respectively. These features contributing to the OAA-SSVM submodels are useful for classification due to their differences among the four pump conditions, which is shown in section V-B. This indicates the OAA-SSVM methodology with the feature sparsity is effective in detecting the multiple faults of the axial piston pump.

VI. CONCLUSION

In this paper, an OAA-SSVM model was proposed to detect faults on the three key lubricating interfaces of axial piston pump. This model takes advantages of the OAA and SSVM algorithm for their faster classification, feature sparsity and classification robustness of dataset with large class imbalance. 20 features extracted from the time domain, frequency domain, and time-frequency domain were used to capture the fault characteristics. Experimental investigations on the benchmark dataset and axial piston pumps were performed to verify the effectiveness of the OAA-SSVM model.

The OAA-SSVM model accuracies of the benchmark dataset and axial piston pump are 96.67% and 95.83%, respectively, which are better than that of the OAA-SVM model. The recall rates of the bearing fault 3 and pump fault 2 decrease by 13.33% and 10.00%, respectively. And the false discovery rates of the normal bearing and normal pump are the highest due to the "Max Wins" criterion of the OAA, which can be reduced by up to 7.58% and 6.24%, respectively.

In addition, the feature sparsity of the OAA-SSVM model was validated by the weight comparison. Results show the proposed methodology is effective in detecting multiple faults of axial piston pumps with the high model accuracy and feature sparsity, and it can also be used in the fault detection of other rotating machineries. Axial piston pumps are complex dynamic systems. In order to deal with the heavy online computation burden problem of these systems, the parity-based fault detection approach would be the future work.

ACKNOWLEDGMENT

The authors would like to thank for code from Jordan Frecon. The authors would like to thank the following people: Z. Ye, H. Shi, and P. Wu in Ningbo Hilead Hydraulic Company, Ltd., for their help in preparing the pumps and performing the tests.

REFERENCES

[1] T. Lin, S. Zhou, Q. Chen, and S. Fu, "A novel control strategy for an energy saving hydraulic system with near-zero overflowing energy-loss," *IEEE Access*, vol. 6, pp. 33810–33818, 2018.
[2] M. Cheng, J. Zhang, B. Xu, R. Ding, and J. Wei, "Decoupling compensation for damping improvement of the electrohydraulic control system with multiple actuators," *IEEE/ASME Trans. Mechatronics*, vol. 23, no. 3, pp. 1383–1392, Jun. 2018.
[3] C. Liu, Y. Liu, X. Liu, G. Yang, X. Zhao, and W. Quan, "Electro-hydraulic servo plate-inclined plunger hydraulic transformer," *IEEE Access*, vol. 4, pp. 8608–8616, 2016.
[4] X. Zhao, S. Zhang, C. Zhou, Z. Hu, R. Li, and J. Jiang, "Experimental study of hydraulic cylinder leakage and fault feature extraction based on wavelet packet analysis," *Comput. Fluids*, vol. 106, pp. 33–40, Jan. 2015.
[5] S. Wang, J. Xiang, Y. Zhong, and H. Tang, "A data indicator-based deep belief networks to detect multiple faults in axial piston pumps," *Mech. Syst. Signal Process.*, vol. 112, pp. 154–170s, Nov. 2018
[6] Q. Zhang, X. Kong, Z. Huang, B. Yu, and G. Meng, "Fluid-structure-interaction analysis of an aero hydraulic pipe considering friction coupling," *IEEE Access*, vol. 7, pp. 26665–26677, 2019.
[7] S. Ye, J. H. Zhang, B. Xu, S. Q. Zhu, J. W. Xiang, and H. S. Tang, "Theoretical investigation of the contributions of the excitation forces to the vibration of an axial piston pump," *Mech. Syst. Signal Proc.*, vol. 129, pp. 201–217, Aug. 2019.
[8] J. H. Zhang, S. Q. Xia, S. G. Ye, B. Xu, S. Q. Zhu, J. W. Xian, and H. S. Tang, "Sound quality evaluation and prediction for the emitted noise of axial piston pumps," *Appl. Acoust.*, vol. 145, pp. 27–40, Feb. 2019.
[9] J. Jiang, K. Wang, Z. Wang, and Y. Sun, "The impact of bushing thickness on the piston/cylinder interface in axial piston pump," *IEEE Access*, vol. 7, pp. 24971–24977, 2019.
[10] I. Jaroslav and I. Monika, *Hydrostatic Pumps And Motors*. New Delhi, India: Academia Book International, 2001.
[11] S. Q. Xia, J. H. Zhang, S. G. Ye, B. Xu, J. W. Xiang, and H. S. Tang, "A mechanical fault detection strategy based on the doubly iterative empirical mode decomposition," *Appl. Acoust.*, vol. 155, pp. 346–357, Dec. 2019.
[12] L. Wen, X. Li, L. Gao, and Y. Zhang, "A new convolutional neural network-based data-driven fault diagnosis method," *IEEE Trans. Ind. Electron.*, vol. 65, no. 7, pp. 5990–5998, Jul. 2018.
[13] C. Lu, Y. Wang, M. Ragulskis, and Y. Cheng, "Fault diagnosis for rotating machinery: A method based on image processing," *PLoS ONE*, vol. 11, no. 10, 2016, Art. no. e0164111.
[14] P. Casoli, A. Bedotti, F. Campanini, and M. Pastori, "A methodology based on cyclostationary analysis for fault detection of hydraulic axial piston pumps," *Energies*, vol. 11, no. 7, p. 1874, Jul. 2018.
[15] Y. Lan, J. W. Hu, J. H. Huang, L. K. Niu, X. H. Zeng, X. Y. Xiong, and B. Wu, "Fault diagnosis on slipper abrasion of axial piston pump based on extreme learning machine," *Measurement*, vol. 124, pp. 378–385, Aug. 2018.
[16] S. Wang, J. Xiang, H. Tang, X. Liu, and Y. Zhong, "Minimum entropy deconvolution based on simulation-determined band pass filter to detect faults in axial piston pump bearings," *ISA Trans.*, vol. 88, pp. 186–198, May 2019.
[17] L. Wang and J. Xiang, "A two-stage method using spline-kernelled chirplet transform and angle synchronous averaging to detect faults at variable speed," *IEEE Access*, vol. 7, pp. 22471–22485, 2019.
[18] J. Sun, H. Li, and B. Xu, "Prognostic for hydraulic pump based upon DCT-composite spectrum and the modified echo state network," *SpringerPlus*, vol. 5, no. 1, p. 1293, 2016.
[19] Z. Zhao, M. Jia, M. Wang, and S. Wang, "Intermittent chaos and sliding window symbol sequence statistics-based early fault diagnosis for hydraulic pump on hydraulic tube tester," *Mech. Syst. Signal Process.*, vol. 23, pp. 1573–1585, Jul. 2009.
[20] C. Lu, S. Wang, and C. Zhang, "Fault diagnosis of hydraulic piston pumps based on a two-step EMD method and fuzzy C-means clustering," *Proc. Inst. Mech. Eng. C, J. Eng. Mech. Eng. Sci.*, vol. 230, no. 16, pp. 2913–2928, 2016.

[21] W. Jiang, Z. Zheng, Y. Zhu, and Y. Li, "Demodulation for hydraulic pump fault signals based on local mean decomposition and improved adaptive multiscale morphology analysis," *Mech. Syst. Signal Process.*, vols. 58–59, pp. 179–205, Jun. 2015.
[22] J. Du, S. Wang, and H. Zhang, "Layered clustering multi-fault diagnosis for hydraulic piston pump," *Mech. Syst. Signal Process.*, vol. 36, pp. 487–504, Apr. 2013.
[23] K. Li, R. Zhang, F. Li, L. Su, H. Wang, and P. Chen, "A new rotation machinery fault diagnosis method based on deep structure and sparse least squares support vector machine," *IEEE Access*, vol. 7, pp. 26571–26580, 2019.
[24] S. Chen, J. Cao, and Z. Huang, "Weighted linear loss projection twin support vector machine for pattern classification," *IEEE Access*, vol. 7, pp. 57349–57360, 2019.
[25] M. Zeng, Y. Yang, S. R. Luo, and J. S. Cheng, "One-class classification based on the convex hull for bearing fault detection," *Mech. Syst. Signal Proc.*, vol. 81, pp. 274–293, Dec. 2016.
[26] J. Spilka, J. Frecon, R. Leonarduzzi, N. Pustelnik, P. Abry, and M. Doret, "Sparse support vector machine for intrapartum fetal heart rate classification," *IEEE J. Biomed. Health Inform.*, vol. 21, no. 3, pp. 664–671, May 2017.
[27] Y. Wang, J. Xiang, R. Markert, and M. Liang, "Spectral kurtosis for fault detection, diagnosis and prognostics of rotating machines: A review with applications," *Mech. Syst. Signal Process.*, vols. 66–67, pp. 679–698, 2016.
[28] Z. B. Yang, M. Radzienski, P. Kudela, and W. Ostachowicz, "Fourier spectral-based modal curvature analysis and its application to damage detection in beams," *Mech. Syst. Signal Process*, vol. 84, pp. 763–781, Feb. 2017.
[29] Z. B. Yang, Y. N. Wang, H. Zuo, X. W. Zhang, Y. Xie, and X. F. Chen, "The Fourier spectral Poincare map method for damage detection via single type of measurement," *Measurment*, vol. 113, pp. 22–37, Jan. 2018.
[30] X. W. Zhang, C. X. Wang, J. Liu, R. Q. Yan, H. R. Cao, and X. F. Chen, "Robust active control based milling chatter suppression with perturbation model via piezoelectric stack actuators," *Mech. Syst. Signal Proc.*, vol. 120, pp. 808–835, Apr. 2019.
[31] S. Wang, X. Chen, I. W. Selesnick, Y. Guo, C. Tong, and X. Zhang, "Matching synchrosqueezing transform: A useful tool for characterizing signals with fast varying instantaneous frequency and application to machine fault diagnosis," *Mech. Syst. Signal Process.*, vol. 100, pp. 242–288, Feb. 2018.
[32] C. X. Wang, X. W. Zhang, J. X. Liu, R. Q. Yan, H. R. Cao, and X. F. Chen, "Multi harmonic and random stiffness excitation for milling chatter suppression," *Mech. Syst. Signal Proc.*, vol. 120, pp. 777–792, Apr. 2019.
[33] Y. Wang, R. Markert, J. Xiang, and W. Zheng, "Research on variational mode decomposition and its application in detecting rub-impact fault of the rotor system," *Mech. Syst. Signal Process.*, vols. 60–61, pp. 243–251, Aug. 2015.
[34] *The Case Western Reserve University Bearing Data Center Website*. [Online]. Available: http://csegroups.case.edu/bearingdatacenter/home
[35] J. H. Zhang, S. Q. Xia, S. G. Ye, B. Xu, W. Song, S. Q. Zhu, H. S. Tang, and J. W. Xiang, "Experimental investigation on the noise reduction of an axial piston pump using free-layer damping material treatment," *Appl. Acoust.*, vol. 139, pp. 1–7, Oct. 2018.

SHIQI XIA received the B.S. degree in mechanical manufacturing and automation from Central South University, Changsha, China, in 2015. He is currently pursuing the Ph.D. degree in mechatronic control engineering with Zhejiang University.

His research interests include fluid power components and systems, vibration and noise reduction, fault diagnosis, and signal processing.

JUNHUI ZHANG received the Ph.D. degree in fluid power transmission and control from Zhejiang University, Hangzhou, China, in 2012.

He is currently an Associate Research Fellow with the State Key Laboratory of Fluid Power and Mechatronic Systems, Zhejiang University. His research interests include noise reduction of hydraulic pumps, fluid power components and systems, and mechatronic systems design.

SHAOGAN YE received the Ph.D. degree in fluid power transmission and control from Zhejiang University, Hangzhou, China, in 2016.

He is currently an Assistant Professor with Xiamen University. His research interests include noise reduction of hydraulic pumps, fluid power components and systems, and mechatronic systems design.

BING XU received the Ph.D. degree in fluid power transmission and control from Zhejiang University, Hangzhou, China, in 2001.

He is currently a Professor and a Doctoral Tutor with the School of Mechanical Engineering, Zhejiang University, where he is currently the Deputy Director of the State Key Laboratory of Fluid Power and Mechatronic Systems. His research interests include fluid power components and systems, mechatronics systems design, energy saving, and motion control for mobile machinery.

WEIDI HUANG received the Ph.D. degree in mechanical manufacturing and automation from Zhejiang University, Hangzhou, China, in 2018.

He is currently a Postdoctoral Researcher with the State Key Laboratory of Fluid Power and Mechatronic Systems, Zhejiang University. His research interests include rotor dynamics and fault diagnosis of axial piston pump.

JIAWEI XIANG (M'19) received the Ph.D. degree from Xi'an Jiaotong University, Xi'an, China, in 2006.

He is currently a Professor with the College of Mechanical and Electrical Engineering, Wenzhou University, China. His research interests include finite-element methods, phononic/photonics crystal materials and devices, health monitoring of mechanical systems using numerical simulation, signal processing, and artificial intelligence techniques.